CrystEngComm

PAPER

Cite this: *CrystEngComm*, 2014, **16**, 8832

Sustainable processing of waste polypropylene to produce high yield valuable Fe/carbon nanotube nanocomposites†

Junhao Zhang,[ac] Longmei Zhang,[a] Huan Yang,[b] Qinghong Kong,*[b] Yuanjun Liu[a] and Aihua Yuan*[a]

Received 23rd May 2014,
Accepted 28th July 2014

DOI: 10.1039/c4ce01064g

www.rsc.org/crystengcomm

With the increasingly serious environmental contamination and energy crisis, it is highly necessary that polyolefin-based waste plastics are converted into valuable materials by innovative upcycling processes. This study presents an environmentally benign and solvent-free autogenic process to produce sponge-like Fe/carbon nanotube nanocomposites by catalytic pyrolysis of waste polypropylene (PP) at 600 °C. The composition and morphology of the products were characterized by powder X-ray diffraction (XRD), Raman spectroscopy, X-ray photoelectron spectroscopy (XPS), field-emission scanning electron microscopy (FESEM), and transmission electron microscopy (TEM). The results show that the products are Fe/carbon nanotube nanocomposites with sponge-like structures, and the diameter of the carbon nanotubes is about 30 nm while the diameter of the Fe nanoparticles in the carbon nanotubes is also about 30 nm, which illustrates that the size of the Fe nanoparticles determines the diameter of the carbon nanotubes. Nitrogen adsorption–desorption measurements indicate that the Brunauer–Emmett–Teller (BET) surface area is calculated to be 197.6 $m^2\ g^{-1}$, and the Barrett–Joyner–Halenda (BJH) adsorption cumulative volume of pores is up to 0.2860 $cm^3\ g^{-1}$. Magnetic measurements at room temperature indicate that the values of saturation magnetization (62.7 emu g^{-1}) and coercivity (187.3 Oe) of the sponge-like Fe/carbon nanotube nanocomposites are different from those of bulk Fe due to the broad distribution of carbon nanotubes and the small size of the Fe nanoparticles.

1. Introduction

In recent years, increasing attention has been focused on carbon-encapsulated magnetic nanostructures, which contain two components: the magnetic core/filler and the non-magnetic carbon matrix/shell.[1,2] Due to its good chemical and thermal stability, a carbon layer can act as a protective barrier to prevent oxidation and degradation of the magnetic performance of metallic particles in harsh environments such as acidic or basic media, and can also reduce the magnetic coupling between individual particles to inhibit agglomeration. Additionally, carbon has good hydrophilic and biocompatible properties, which makes it possible to load other functional molecules. Therefore, carbon-encapsulated magnetic nanoparticles are promising candidates for applications in magnetic resonance imaging (MRI),[3] ultrahigh-density magnetic recording media,[4] integrated diagnosis and therapeutics,[5] drug delivery,[6] catalysis,[7] environmental protection,[8] and electromagnetic (EM) wave absorption.[9]

To date, numerous techniques have been developed to synthesize carbon-encapsulated magnetic nanoparticles.[10–15] Cai prepared carbon-encapsulated Fe_3O_4 nanoparticles by first introducing an amorphous carbon coating on the Fe_3O_4 surface using the hydrothermal method and then heating the as-prepared nanoparticles in an N_2 atmosphere.[16] Tsutomu synthesized onion-like carbon-encapsulated Co, Ni, and Fe magnetic nanoparticles by using a pulsed plasma in a liquid.[17] Zhao reported that ordered mesoporous Fe_2O_3@C encapsulates with novel nanoarchitectures have been designed and fabricated by an ammonia-atmosphere pre-hydrolysis post-synthetic route.[18] Bystrzejewski reported that carbon-encapsulated iron nanoparticles were produced by carbon arc discharge.[19] Oh prepared magnetic particle-embedded porous carbon composites by one-step pyrolysis of a metal–organic framework.[20] However, it is still a great challenge to develop

[a] *School of Environmental and Chemical Engineering, Jiangsu University of Science and Technology, Zhenjiang, Jiangsu 212018, China. E-mail: aihua.yuan@just.edu.cn; Fax: +86 511 84407381; Tel: +86 511 84401181*
[b] *School of the Environment and Safety Engineering, Jiangsu University, Zhenjiang, Jiangsu 212013, China. E-mail: kongqh@mail.ujs.edu.cn*
[c] *CAS Key Laboratory of Materials for Energy Conversion, University of Science and Technology of China, Hefei, Anhui 230026, China*
† The authors declare no competing financial interest.

simple, green and economical synthetic strategies for carbon-encapsulated magnetic nanoparticles with designed chemical components and controlled morphologies.

Recently, the disposal of waste plastics has been an important concern for society because of the widespread use of different plastic polymers.[21–24] To reduce the impact of plastics on the environment, it is highly necessary to design and facilitate the means to recycle more, and typically, waste reduction, recycling (mechanical, chemical, and thermal) as well as landfilling are considered as common solutions. Since plastics are not biodegradable, it is not an effective solution to deal with them in landfills. The most common alternative for the treatment of waste plastics in many countries is incineration accompanied by energy recovery.[25] This option is often rejected by society because of the risk of emission of toxic compounds, such as dioxins and furans. Nowadays, extensive collection, transportation, separation, and recycling facilities are available for processing waste thermoplastic products. Unfortunately, by mixing different waste plastics, homogeneous materials suitable for making quality products may not be obtained. The problem of mixed plastics has been partially solved by separation technologies such as flotation[26] and plasma gasification.[27] However, these multistep recycling processes are not cost-effective.

Among the different alternatives for plastic waste treatment, the most promising seems to be chemical recycling as it has the lowest environmental impact and the highest possible profitability. There has been recent interest in applying the technology to the gasification of waste plastics to yield smaller molecules, usually liquids or gases, that are suitable as feedstocks to produce new petrochemicals and plastics. However, this requires the construction of large plants to be profitable, the processes require a high reaction temperature (more than 600 °C and even up to 900 °C),[28–30] and there is a broad range of products. Due to the fact that carbon is the major constituent of plastics, waste plastics can provide a carbon source for producing value-added carbon-based products. For example, Kartel *et al.*[31] prepared activated carbon with a BET surface area of 1030 $m^2\ g^{-1}$ and an effective pore size of 1.8 nm using polyethylene terephthalate as the carbon source at 800 °C. However, the yield of solid carbon was only 22%. Williams *et al.*[32] reported that hydrogen and high-value carbon nanotubes were derived from waste plastic using a pyrolysis-reforming technology. The results show that around 94.4 mmol $H_2\ g^{-1}$ plastic was obtained from the pyrolysis-reforming of HDPE waste in the presence of a Ni–Mn–Al catalyst and steam at 800 °C, and about 33.8 wt.% filamentous carbon was prepared from the pyrolysis of motor oil containers in the presence of the Ni–Mn–Al catalyst without steam at 800 °C. Recently, a simple one-step process without solvents was used to convert PE and other waste plastics (such as polyethylene terephthalate, polypropylene and polystyrene) into carbon materials.[33–37] This approach is efficient and scalable, but the reaction temperatures are high and the yields are low. In order to develop an economically applicable process for industrial use, it is necessary to improve the production yield of solid carbon under mild conditions. To the best of our knowledge, few reports exist for the synthesis of Fe/carbon nanocomposites using waste plastics as feedstocks. As a result, converting waste plastics to Fe/carbon nanocomposites on a large scale at relatively low temperature still remains a great challenge.

Herein, we introduce a creative method to convert waste PP to sponge-like Fe/carbon nanotube nanocomposites by manipulating the formation of carbon on the catalyst. The process involves thermal decomposition of waste polypropylene in the presence of catalysts at 600 °C in a closed reactor, which is simple, reproducible and affordable. The composition, morphology, and structure of the as-obtained Fe/carbon nanotube nanocomposites were characterized using advanced structural, spectroscopic, and imaging techniques. This invention presents an opportunity to use waste plastics as raw materials for the production of Fe/carbon nanotube nanocomposites. With their unique properties, Fe/carbon nanotube nanocomposites will undoubtedly have many applications in the areas of electronics, biosensing and energy storage, and have potential as reinforced composites for aeroplanes.

2. Experimental section

In a typical procedure, waste PP (1.0 g), ferrocene (1.0 g) and NaN_3 (1.0 g) were loaded into a 20 mL stainless steel autoclave. The autoclave was tightly sealed and heated in an electronic furnace. The temperature of the furnace was increased to 600 °C over 60 min and maintained at 600 °C for 12 h. Then, the autoclave was allowed to cool to room temperature naturally. It was found that the final products in the autoclave were black precipitates and residual gases. The black precipitates were collected and washed with distilled water and ethanol several times. After that, the products were dried in a vacuum box at 50 °C for 4 h, and collected for characterization.

The as-prepared products were characterized by powder X-ray diffraction (XRD) employing a Rigaku (Japan) D/max-γA X-ray diffractometer equipped with graphite-monochromatized Cu Kα radiation (λ = 1.54178 Å). The Raman spectra were recorded at ambient temperature on a SPEX 1403 spectrometer with an argon-ion laser at an excitation wavelength of 514.5 nm. X-ray photoelectron spectroscopy (XPS) of the products was performed using a VGESCALABMK X-ray photoelectron spectrometer and non-monochromated Mg Kα radiation as the excitation source. The field-emission scanning electron microscopy (FESEM) images of the products were taken using a field-emission scanning electron microscope (JEOL-6300F). The transmission electron microscopy (TEM) images were taken on a JEOL 2010 high-resolution transmission electron microscope at an acceleration voltage of 200 kV. Energy dispersive spectrometric (EDS) analysis was carried out on an X-ray energy spectrum instrument equipped with an INCA300 (Oxford). The nitrogen adsorption–desorption isotherms and textural properties were determined using a

Beckman Coulter SA3100. The magnetic properties (*M–H* curve) were measured at room temperature on an MPMS XL magnetometer made by Quantum Design Corporation.

3. Results and discussion

To ascertain the components and structures of the products, XRD was used to investigate the crystal phases. Fig. 1 shows the powder XRD pattern of the Fe/carbon nanotube nanocomposites produced by catalytic pyrolysis of waste PP at 600 °C. The sharp diffraction peaks with relatively high peak intensity can be indexed as α-Fe, in agreement with the literature values (Joint Committee on Powder Diffraction Standards (JCPDS), card no. 85-1410). Meanwhile, the broad peak located at about 26.2° can be assigned to amorphous graphite. No other impurity peaks were detected, revealing the high purity of the synthesized products.

Raman spectroscopy can be used to characterize the carbon structures of carbonaceous materials such as graphite and diamond-like carbon, and provides information on the molecular structure and chemical bonding of carbon atoms in carbonized materials. Fig. 2 shows the Raman spectrum of the Fe/carbon nanotube nanocomposites, displaying two similar Raman bands at 1346 cm^{-1} (D band) and 1596 cm^{-1} (G band). More specifically, the two peaks can be attributed to an E_{2g} mode of graphite related to the vibration of sp^2-bonded carbon atoms in a 2D hexagonal lattice (such as in a graphene layer) and an A_{1g} mode of graphite related to the disorder due to the finite particle size effect or lattice distortion of the graphite crystals. The relative intensity ratio of the D–G band, I_D/I_G, can give reliable information on the degree of graphitization. It is found that the Fe/carbon nanotube nanocomposites have a higher I_D/I_G, implying a highly disordered graphitic structure in the carbon nanotubes, and these results are consistent with the XRD pattern.

X-ray photoelectron spectroscopy (XPS) has often been used for the surface characterization of various materials,

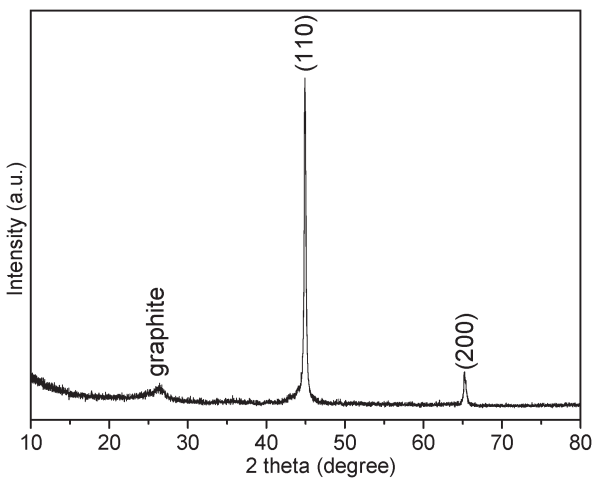

Fig. 1 A typical XRD pattern of Fe/carbon nanotube nanocomposites formed at 600 °C.

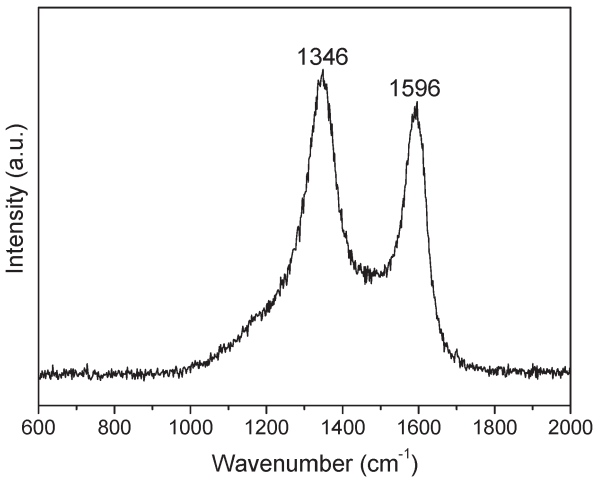

Fig. 2 Raman spectrum of Fe/carbon nanotube nanocomposites formed at 600 °C.

and unambiguous results are readily obtained when the various surface components each contain unique elemental markers. Here, in order to analyze the surface components of the Fe/carbon nanotube nanocomposites, XPS measurements were carried out on the products. The XPS spectra of the Fe/carbon nanotube nanocomposites are shown in Fig. 3. The peaks in the main pattern (Fig. 3a) can mainly be attributed to C1s (285.7 eV), Fe2p (711.0 and 724.8 eV) and their corresponding Auger peaks. However, almost no peaks are detected for the O1s binding energy, suggesting that the products consist of elements C and Fe. Fig. 3b shows that the peaks of Fe2p are weak, which indicates that the Fe nanoparticles may be encapsulated in carbon.

Magnetic materials encapsulated in carbon-based systems have attracted increasing attention due to their electrical and magnetic properties and their variety of potential technological applications. In recent years, there have been a number of studies on iron and carbon composites. In Fig. 4a, another type of Fe/carbon nanocomposite is presented in high morphological yield, and the nanocomposites consist of sponge-like structures. The high-magnification FESEM image in Fig. 4b shows that the nanocomposites are assembled from one-dimensional structures with diameters of about 30 nm and lengths of several micrometers. Careful observation reveals that there are many catalyst nanoparticles at the tops of the one-dimensional structures. The structures were further characterized by TEM. Fig. 5a shows a TEM image of the products, which agrees with the FESEM images. A notable result is that the diameter of the carbon nanotubes is about 30 nm and the diameter of the catalyst nanoparticles is also about 30 nm, which indicates that the size of the Fe nanoparticles determines the diameter of the carbon nanotubes. Fig. 5b shows that the products include some amorphous mesoporous carbon besides the carbon nanotubes. From the TEM images, the carbon nanotubes are bamboo-like structures. The inset image in Fig. 5b is the SAED pattern of the Fe nanoparticles, which suggests that

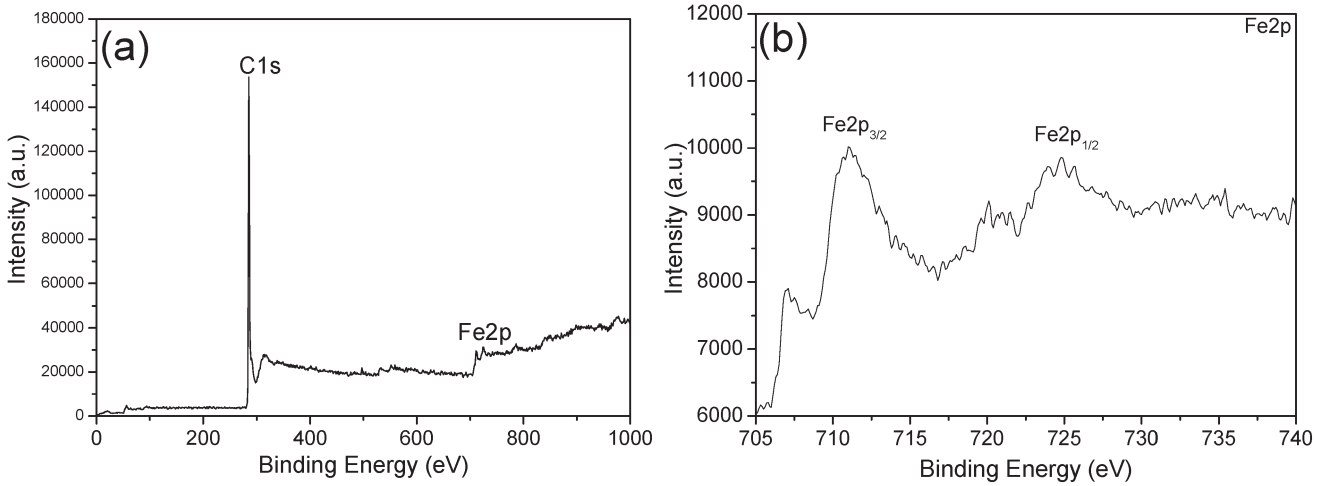

Fig. 3 X-ray photoelectron spectra of Fe/carbon nanotube nanocomposites produced by catalytic pyrolysis of waste PP at 600 °C: (a) wide scan spectrum; (b) high-resolution XPS spectrum of the Fe2p region.

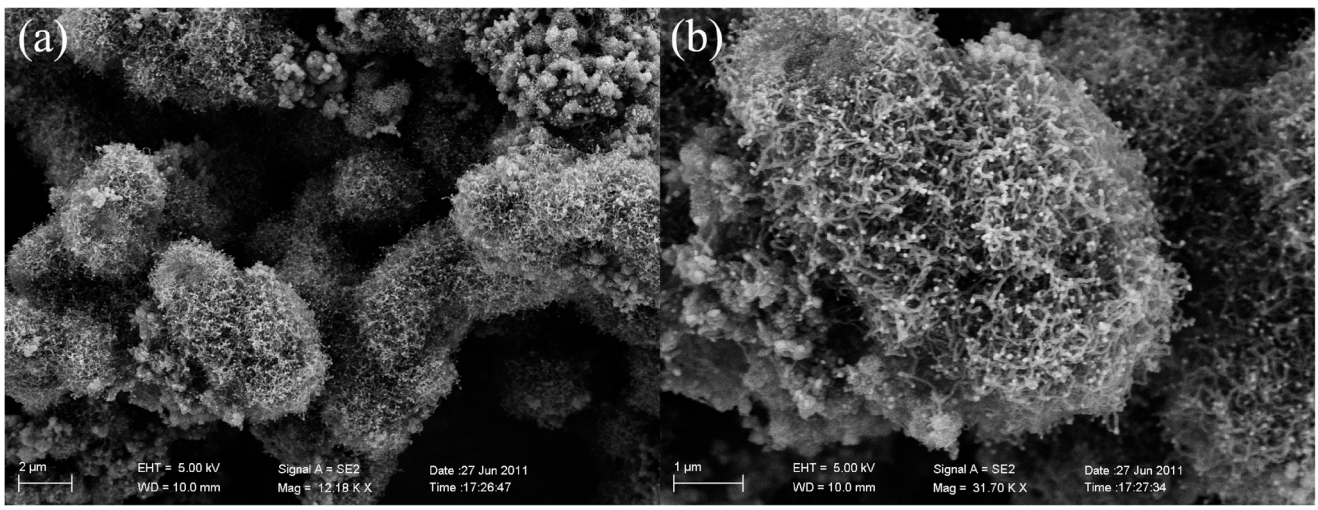

Fig. 4 (a) Low-magnification FESEM image of Fe/carbon nanotube nanocomposites; (b) high-magnification FESEM image of Fe/carbon nanotube nanocomposites.

these Fe nanoparticles have body-centered cubic (bcc) crystal structures. Fig. 5c is a HRTEM image of the wall structures of the carbon nanotubes, which displays clear lattice fringes. The interlayer spacings in the walls are about 0.34 nm, corresponding to the (002) distance of the graphitic carbon lattice. However, the lattice fringes have short-range order, and the carbon nanotubes have some stacking faults, which indicates that the carbon nanotubes have low crystallinity. The results of the EDS analysis (Fig. 5d) confirm that elements Fe and C are present in the nanocomposites. The signals for Cu come from the supporting TEM grid used during measurements.

Nitrogen adsorption–desorption isotherms of the Fe/carbon nanotube nanocomposites formed at 600 °C show a type IV curve, as seen in Fig. 6a. The pore size distribution derived from the adsorption branch using the BJH method shows that the pore size is centered at about 2.3, 3.4 and 30.1 nm (Fig. 6b). The BET surface area is calculated to be 197.6 $m^2\ g^{-1}$, and the BJH adsorption cumulative volume of pores is up to 0.2860 $cm^3\ g^{-1}$ between 1.7 and 300 nm. This value is high compared with that of the carbon nanotubes in our previous report.[38] According to the morphology and structural characteristics, the higher BET surface area can be attributed to the smaller diameters, rough surface and more defects in the carbon nanotubes, and the existence of some amorphous mesoporous carbon.

To understand the possible formation process of the Fe/carbon nanotube nanocomposites, a series of relevant experiments was carried out by altering the experimental parameters. It is obvious that the reaction temperature plays a critical role in the formation of Fe/carbon nanotube nanocomposites. At a reaction temperature of 600 °C, the products are sponge-like Fe/carbon nanotube nanocomposites with high morphological yield. Fig. 7 shows FESEM images of the products obtained at 500 °C and 700 °C. Fig. 7a shows that

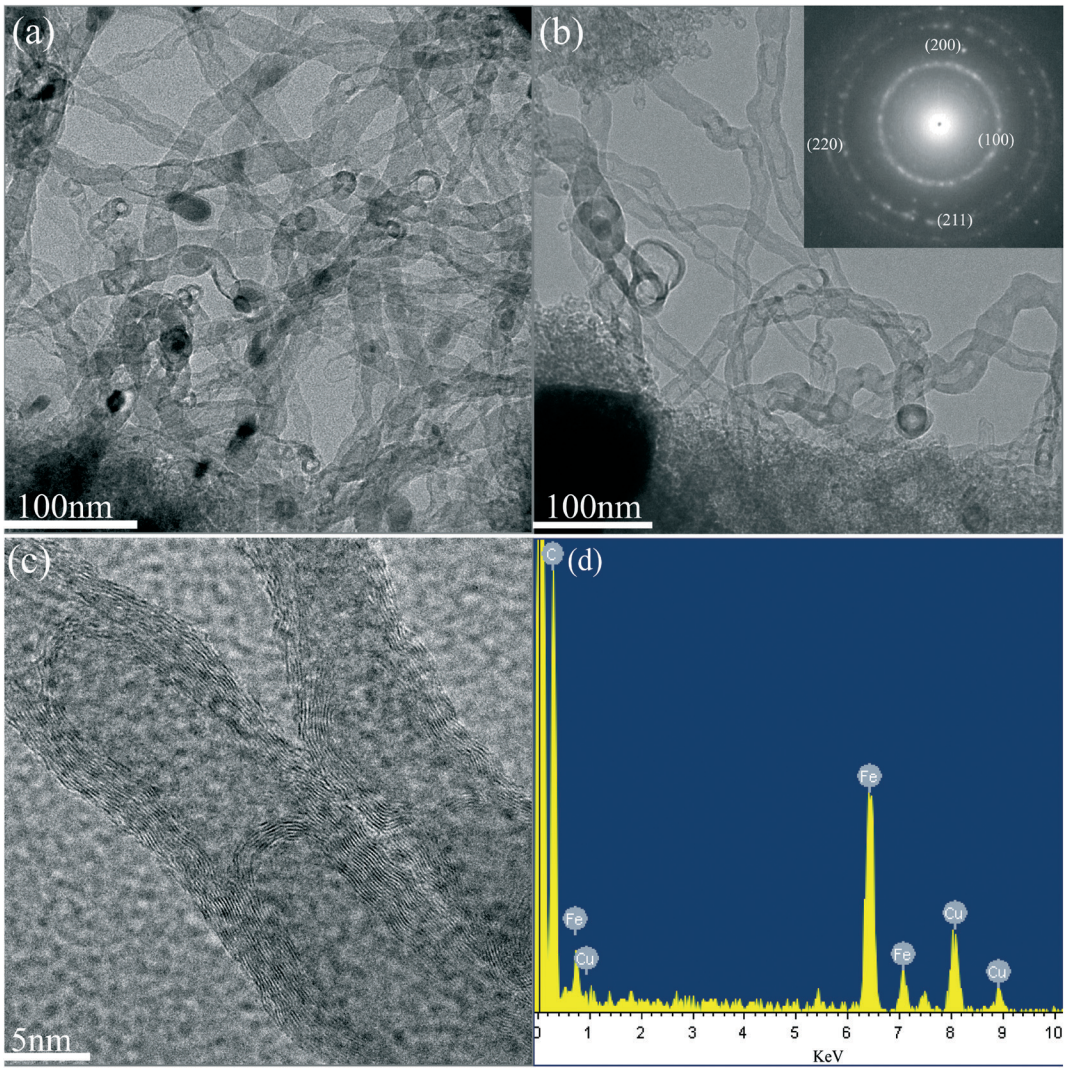

Fig. 5 (a) and (b) TEM images of Fe/carbon nanotube nanocomposites and SAED pattern of Fe nanoparticles (inset in (b)); (c) HRTEM image of the wall structures of the carbon nanotubes in Fe/carbon nanotube nanocomposites; (d) EDS spectrum of Fe/carbon nanotube nanocomposites.

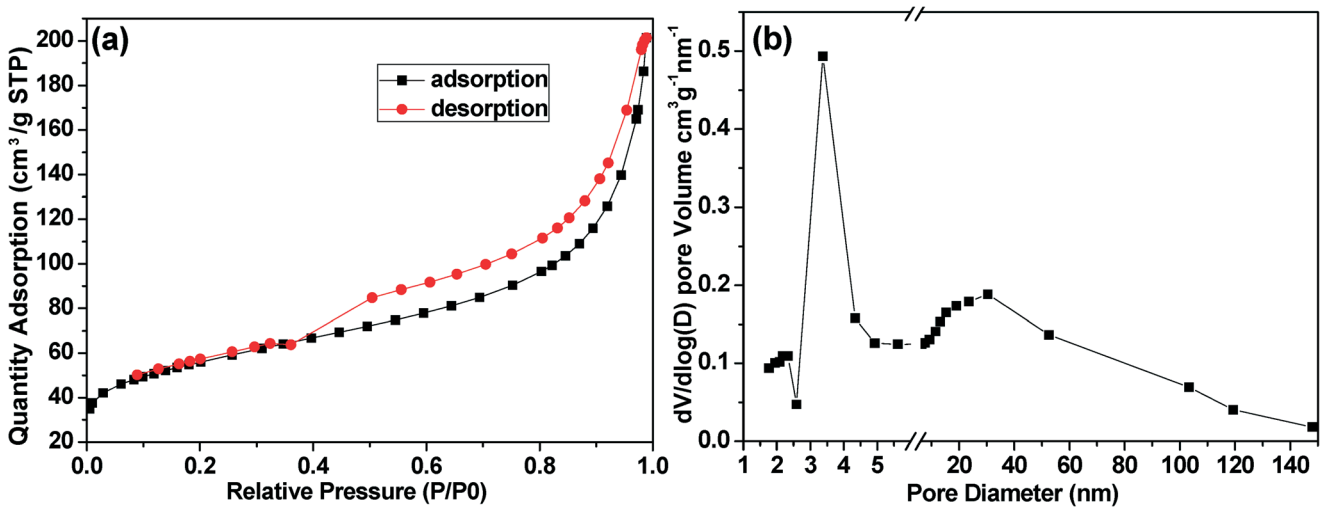

Fig. 6 (a) Typical N_2 adsorption–desorption isotherm of Fe/carbon nanotube nanocomposites formed at 600 °C; (b) pore size distribution of Fe/carbon nanotube nanocomposites formed at 600 °C.

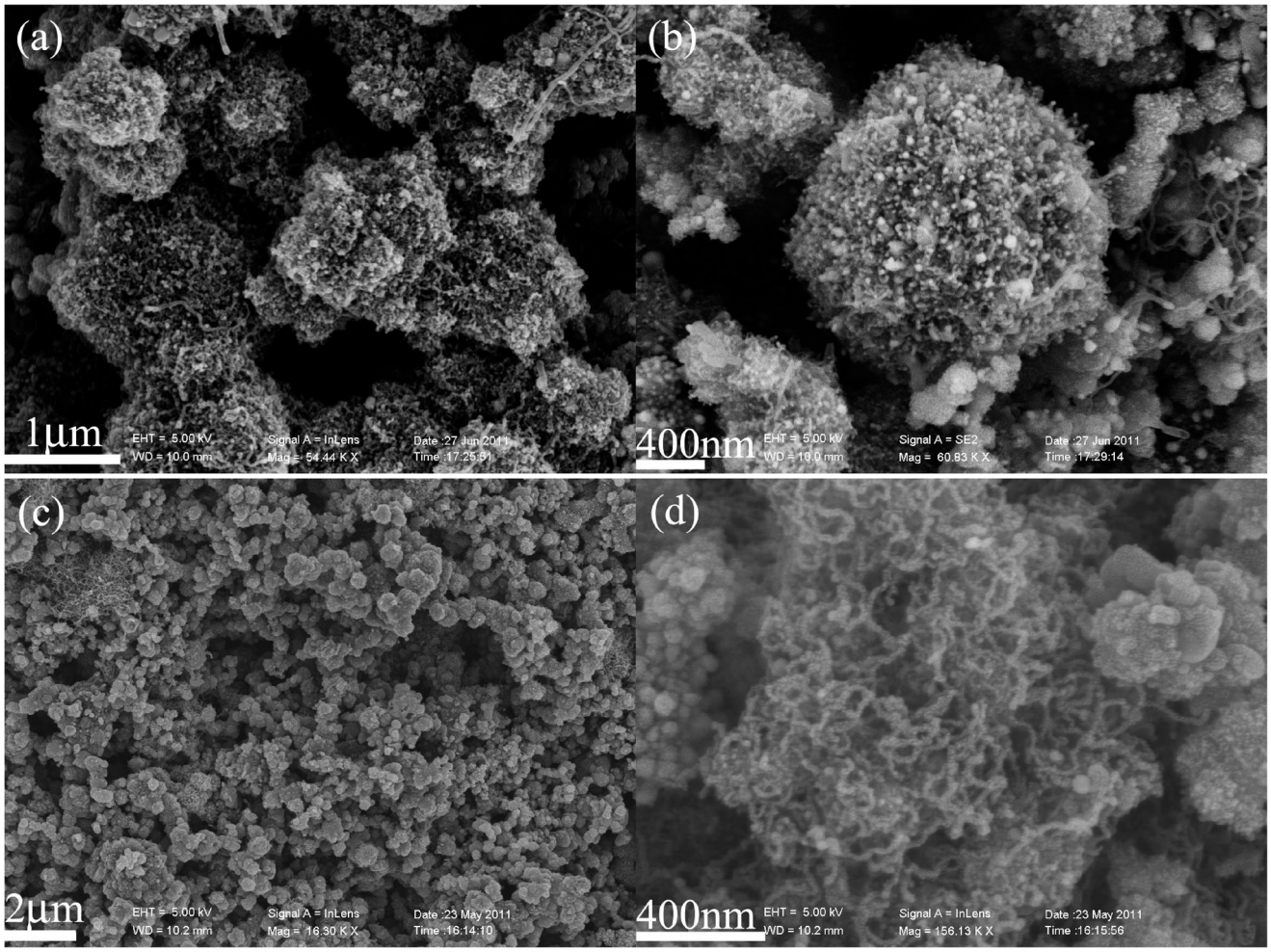

Fig. 7 (a) Low-magnification FESEM image of the products obtained at 500 °C; (b) high-magnification FESEM image of the products obtained at 500 °C; (c) low-magnification FESEM image of the products obtained at 700 °C; (d) high-magnification FESEM image of the products obtained at 700 °C.

the morphology and size of the main products are uniform for a reaction temperature of 500 °C, which is similar to the sponge-like structures in Fig. 4a, and the morphological yield is about 80%. Fig. 7b indicates that the products also consist of some particles and scattered carbon nanotubes. On increasing the reaction temperature to 700 °C, the products are mainly uniform particles with sizes in the range of 200–700 nm, as shown in Fig. 7c. Careful observation reveals that a small number of carbon nanotubes are present in the products, as the high-magnification FESEM image in Fig. 7d shows. Apart from the reaction temperature, the products can also be tuned by varying the reaction atmosphere. From Fig. 8 and 9, it can be seen that the reaction atmosphere influences the compositions and morphologies of the products. When H_2O was used in place of NaN_3, the products were one-dimensional worm-like structures with a diameter of about 580 nm, and some carbon spheres with diameter 1.7 μm were also found in the products, as shown in Fig. 8a. Fig. 9a indicates that the products are composites of C and Fe_3O_4. In this system, PP decomposed to produce small molecular carbonyl compounds as the carbon source in the absence of oxygen, and Fe atoms released by the decomposition of ferrocene acted as the dehydrogenation catalyst. The as-formed Fe atoms reacted with H_2O to form Fe_3O_4 nanoparticles due to the presence of water vapor, and the obtained Fe_3O_4 particles were self-assembled into chain-like structures under the influence of the magnetic dipole interaction. The small molecular carbonyl compounds were carbonized to produce carbon atoms, which precipitated on the surface of the Fe_3O_4 chains to form worm-like structures. When $NaNH_2$ was used in place of NaN_3, the products were nanoflakes and nanoparticles and mainly composed of C and Fe, as shown in Fig. 8b and 9b. The formation mechanism is similar to that using NaN_3. When $NaNH_2$ was used in place of NaN_3, $NaNH_2$ decomposed to release Na, N_2, H_2 and NH_3. Fe atoms were not oxidized in the presence of Na and H_2, which acted as the dehydrogenation catalyst to decompose small molecular carbonyl compounds to form carbon atoms. Carbon atoms were precipitated on the surface of the Fe nanoparticles and formed a thin carbon lamella which reduced the surface energy and prevented the continued growth of the Fe nanoparticles. As there is a large number of

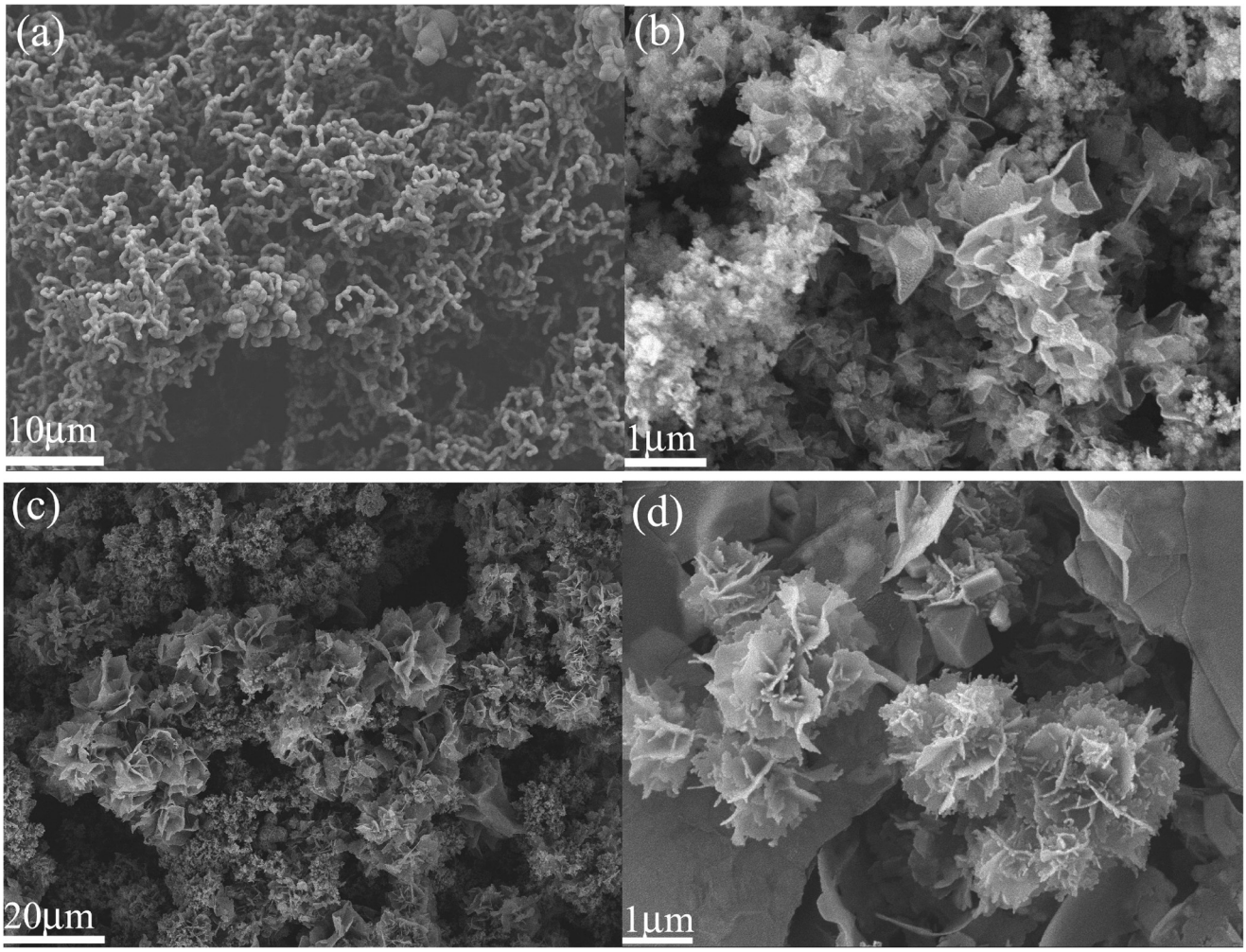

Fig. 8 (a) FESEM image of the products using H_2O in place of NaN_3; (b) FESEM image of the products using $NaNH_2$ in place of NaN_3; (c) FESEM image of the products using $CO(NH_2)_2$ in place of NaN_3; (d) FESEM image of the products using S powder in place of NaN_3.

carbon atoms in the system, the redundant carbon atoms lead to the formation of carbon nanoflakes. When NaN_3 was replaced by $CO(NH_2)_2$, the products were large amounts of flower-like structures assembled from nanoflakes and nanoparticles and mainly composed of C and Fe_3O_4, as shown in Fig. 8c and 9c. In this process, the obtained Fe atoms were oxidized to form Fe_3O_4 particles in the atmosphere of NH_3 and HCNO formed by decomposition of $CO(NH_2)_2$. The formation process of the products is similar to that using $NaNH_2$. When NaN_3 was replaced by S powder, Fig. 8d shows that the products included flower-like spheres, large flakes and polyhedron structures. Fig. 9d reveals that the products were composites of C and FeS. In this process, Fe atoms reacted with S to form FeS particles. Carbon atoms from catalytic carbonization of PP were precipitated to form carbon flakes and flower-like spheres. Consequently, it can be seen that an appropriate atmosphere could facilitate the assembly of sponge-like Fe/carbon nanotube nanocomposites.

The magnetic properties were investigated at room temperature with an applied field from −10 000 Oe to 10 000 Oe. In Fig. 10b, the magnetic hysteresis loop of Fe/carbon nanotube nanocomposites formed at 600 °C shows ferromagnetic behavior with saturation magnetization (M_s), remanent magnetization (M_r), and coercivity (H_c) values of *ca.* 62.7 emu g^{-1}, 6.7 emu g^{-1} and 187.3 Oe, respectively. Compared to results reported elsewhere,[39] the M_s value is smaller than the value of bulk Fe (212 emu g^{-1}). The decrease in the value of M_s found in this work is most likely attributed to the broad distribution of carbon nanotubes, and these carbon nanotubes restrict the possible movement and interactions of the α-Fe nanoparticles. This effect is similar to that of the surfactant existing on the Fe nanoparticles, which leads to a decrease in the M_s value.[40] This may also be attributed to the small size of the Fe nanoparticles (~30 nm). The results of combustion experiments indicate that the calculated Fe to Fe/carbon nanotube nanocomposites mass ratio of the products is about 0.3065. Additionally, Fig. 10a and c show that the saturation magnetization (M_s) values of Fe/carbon nanotube nanocomposites obtained at 500 °C and 700 °C are *ca.* 60.9 emu g^{-1} and 64.9 emu g^{-1}, respectively, which are similar to the value for Fe/carbon nanotube nanocomposites formed at 600 °C. However, the H_c values of Fe/carbon

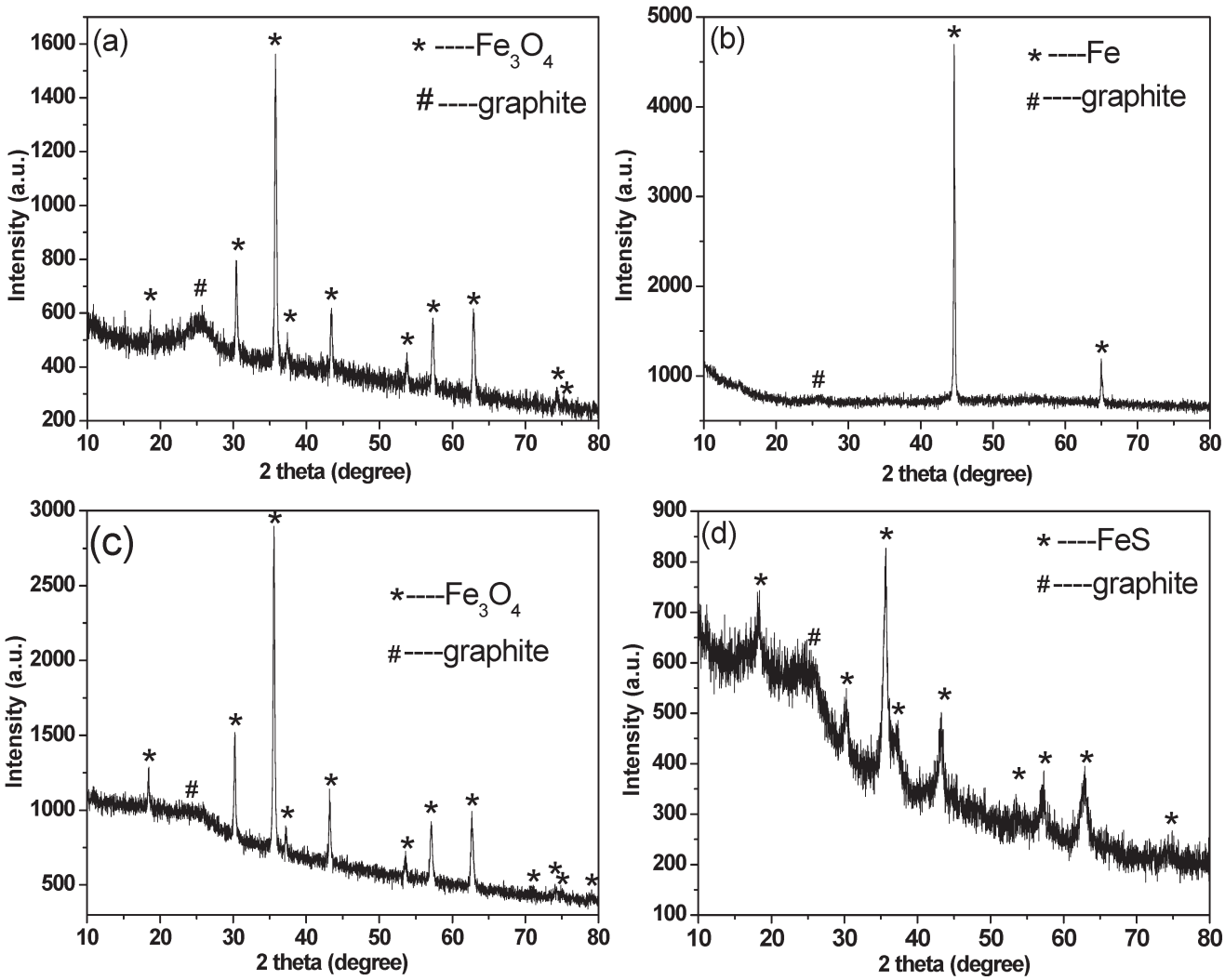

Fig. 9 (a) XRD pattern of the products using H_2O in place of NaN_3; (b) XRD pattern of the products using $NaNH_2$ in place of NaN_3; (c) XRD pattern of the products using $CO(NH_2)_2$ in place of NaN_3; (d) XRD pattern of the products using S powder in place of NaN_3.

nanotube nanocomposites obtained at 500 °C and 700 °C are *ca.* 114.2 Oe and 87.0 Oe, which are smaller than the value (187.3 Oe) for Fe/carbon nanotube nanocomposites formed at 600 °C. The reason for the high H_c value for Fe/carbon nanotube nanocomposites formed at 600 °C might be the high content of magnetic nanoparticles in quasi-one-dimensional arrangement due to the restriction of the carbon nanotubes.[41] Moreover, it was observed that the obtained sample showed no change in magnetic properties after being kept in air for over two months, suggesting that the α-Fe nanoparticles were well-protected by the graphite layers.

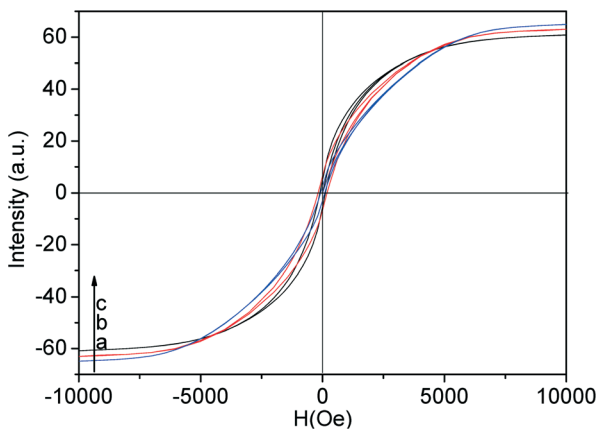

Fig. 10 Magnetic hysteresis loops at room temperature for Fe/carbon nanotube nanocomposites obtained at (a) 500 °C, (b) 600 °C and (c) 700 °C.

4. Conclusions

In summary, Fe/carbon nanotube nanocomposites with sponge-like structures were synthesized through catalytic decomposition of waste PP at 600 °C. The Fe/C nanocomposites were mainly self-assembled from carbon nanotubes and Fe nanoparticles as a result of magnetic interactions. The diameter of the carbon nanotubes is about 30 nm and the diameter of the Fe nanoparticles in the carbon nanotubes is also about 30 nm. The BET surface area is calculated to be

197.6 m^2 g^{-1}, and the BJH adsorption cumulative volume of pores is up to 0.2860 cm^3 g^{-1}. Magnetic hysteresis loop measurement shows that the sponge-like Fe/carbon nanotube nanocomposites display ferromagnetic properties at room temperature, and the saturation magnetization value (62.7 emu g^{-1}) is lower than that of bulk Fe, which can be attributed to the broad distribution of carbon nanotubes and the reduced size of the Fe nanoparticles. The high coercivity (H_c) value (187.3 Oe) might result from the high content of magnetic nanoparticles in quasi-one-dimensional arrangement due to the restriction of the carbon nanotubes.

Acknowledgements

The work was financially supported by Natural Science Foundation of Jiangsu Province (no. BK20141293, BK2012276), Natural Science Foundation of the Higher Education Institutions of Jiangsu Province (no. 13KJB430012), the Opening Project of CAS Key Laboratory of Materials for Energy Conversion (no. KF 2014006), Natural Science Foundation of China (no. 51203069), and Qinglan project.

References

1 C. Yu, Y. Sun, X. M. Fan, Z. B. Zhao and J. S. Qiu, *Part. Part. Syst. Charact.*, 2013, **30**, 637.
2 H. B. Geng, Q. Zhou, Y. Pan, H. W. Gu and J. W. Zheng, *Nanoscale*, 2014, **6**, 3889.
3 I. A. Choi, Y. Li, D. J. Kim, M. Pal, J. H. Cho, K. Lee, M. H. Jung, C. Lee and W. S. Seo, *Chem. – Asian J.*, 2013, **8**, 290.
4 X. W. Wei, G. X. Zhu, C. J. Xia and Y. Ye, *Nanotechnology*, 2006, **17**, 4307.
5 W. S. Seo, J. H. Lee, X. M. Sun, Y. Suzuki, D. Mann, Z. Liu, M. Terashima, P. C. Yang, M. V. McConnell, D. G. Nishimura and H. J. Dai, *Nat. Mater.*, 2006, **5**, 971.
6 X. J. Fan, G. Z. Jiao, L. Gao, P. F. Jin and X. Li, *J. Mater. Chem. B*, 2013, **1**, 2658.
7 G. G. Liu, F. He, J. Zhang, L. J. Li, F. J. Li, L. X. Chen and Y. Huang, *Appl. Catal., B*, 2014, **150**, 515.
8 Z. X. Wu, W. Li, P. A. Webley and D. Y. Zhao, *Adv. Mater.*, 2012, **24**, 485.
9 Y. Yang, Z. Guo, H. Zhang, D. Q. Huang, J. L. Gu, Z. H. Huang, F. Y. Kang, T. A. Hatton and G. C. Rutledge, *J. Appl. Polym. Sci.*, 2013, **127**, 4288.
10 X. Zhang, O. Allou, J. H. Zhu, Q. L. He, Z. P. Luo, H. A. Colorado, N. Haldolaarachchige, D. P. Young, T. D. Shen, S. Y. Wei and Z. H. Guo, *RSC Adv.*, 2013, **3**, 9453.
11 T. Ren, Y. Si, J. M. Yang, B. Ding, X. X. Yang, F. Hong and J. Y. Yu, *J. Mater. Chem.*, 2012, **22**, 15919.
12 N. Aguiló-Aguayo, Z. Y. Liu, E. Bertran and J. Yang, *J. Phys. Chem. C*, 2013, **117**, 19167.
13 C. N. He, S. Wu, N. Q. Zhao, C. S. Shi, E. Z. Liu and J. J. Li, *ACS Nano*, 2013, **7**, 4459.
14 M. del. C. Gimenez-Lopez, A. L. Torre, M. W. Fay, P. D. Brown and A. N. Khlobystov, *Angew. Chem., Int. Ed.*, 2013, **52**, 2051.
15 P. Lukanov, V. K. Anuganti, Y. Krupskaya, A. M. Galibert, B. Soula, C. Tilmaciu, A. H. Velders, R. Klingeler, B. Büchner and E. Flahaut, *Adv. Funct. Mater.*, 2011, **21**, 3583.
16 H. Y. Niu, Y. X. Wang, X. L. Zhang, Z. F. Meng and Y. Q. Cai, *ACS Appl. Mater. Interfaces*, 2012, **4**, 286.
17 A. Zhypargul, O. Emil, I. Chihiro, S. G. Hullathy, S. Saadat, L. L. Chen and M. Tsutomu, *Carbon*, 2012, **50**, 1776.
18 Z. X. Wu, W. Li, P. A. Webley and D. Y. Zhao, *Adv. Mater.*, 2012, **24**, 485.
19 M. Bystrzejewski, O. Labedz, W. Kaszuwara, A. Huczko and H. Lange, *Powder Technol.*, 2013, **246**, 7.
20 H. J. Lee, W. Cho, E. Lim and M. Oh, *Chem. Commun.*, 2014, **50**, 5476.
21 D. P. Serrano, J. Aguado and J. M. Escola, *ACS Catal.*, 2012, **2**, 1924.
22 C. W. Zhuo and Y. A. Levendis, *J. Appl. Polym. Sci.*, 2014, **131**, 39931.
23 C. F. Wu, Z. C. Wang, L. Z. Wang, P. T. Williams and J. Huang, *RSC Adv.*, 2012, **2**, 4045.
24 J. N. Sahu, K. K. Mahalik, H. K. Nam, T. Y. Ling, T. S. Woon, M. S. B. Rahman, Y. K. Mohanty, N. S. Jayakumar and S. S. Jamuar, *Environ. Prog. Sustainable Energy*, 2014, **33**, 298.
25 P. A. Wager, M. Schluep, E. Muller and R. Gloor, *Environ. Sci. Technol.*, 2012, **46**, 628.
26 N. Fraunholcz, *Miner. Eng.*, 2004, **17**, 261.
27 H. S. Park, C. G. Kim and S. J. Kim, *J. Ind. Eng. Chem.*, 2006, **12**, 216.
28 S. K. Ouiminga, T. Rogaume, M. Sougoti, J. M. Commandre and J. Koulidiati, *J. Anal. Appl. Pyrolysis*, 2009, **86**, 260.
29 S. H. Jung, M. H. Cho, B. S. Kang and J. S. Kim, *Fuel Process. Technol.*, 2010, **91**, 277.
30 A. H. Lu, W. C. Li, E. L. Salabas, B. Spliethoff and F. Schuth, *Chem. Mater.*, 2006, **18**, 2086.
31 M. T. Kartel, N. V. Sych, M. M. Tsyba and V. V. Strelko, *Carbon*, 2006, **44**, 1019.
32 C. F. Wu, M. A. Nahil, N. Miskolczi, J. Huang and P. T. Williams, *Environ. Sci. Technol.*, 2014, **48**, 819.
33 J. C. Acomb, C. F. Wu and P. T. Williams, *Appl. Catal., B*, 2014, **147**, 571.
34 S. Y. Sawant, R. S. Somani, A. B. Panda and H. C. Bajaj, *ACS Sustainable Chem. Eng.*, 2013, **1**, 1390.
35 J. H. Zhang, B. Yan, S. Wan and Q. H. Kong, *Ind. Eng. Chem. Res.*, 2013, **52**, 5708.
36 J. A. Onwudili, N. Insura and P. T. Williams, *J. Energy Inst.*, 2013, **86**, 227.
37 J. H. Zhang, B. Yan, H. Wu and Q. H. Kong, *RSC Adv.*, 2014, **4**, 6991.
38 J. H. Zhang, J. Du, Y. T. Qian and S. L. Xiong, *Mater. Res. Bull.*, 2010, **45**, 15.
39 Y. Leconte, S. Veintemillas-Verdaguer, M. P. Morales, R. Costo, I. Rodriguez, P. Bonville, B. Bouchet-Fabre and N. Herlin-Boime, *J. Colloid Interface Sci.*, 2007, **313**, 511.
40 S. Ghosh, W. Jiang, J. D. McClements and B. S. Xing, *Langmuir*, 2011, **27**, 8036.
41 F. Zhao, H. Y. Duan, W. G. Wang and J. Wang, *Phys. B*, 2012, **407**, 2495.

